# New scanning gonio-photometer for extended BRTF measurements

Peter Apian-Bennewitz[a]

[a]pab advanced technologies Ltd, Freiburg, Germany

## ABSTRACT

Measured data of the angular distribution of light scattering by surfaces (bi-directional-reflection-transmittance-function, BRTF) has use in many fields: among them are stray light in lens design, projection screens,[1] advanced architectural glazings and validating of surface and material models. Existing measurement devices either use cameras to capture multiple outgoing directions (*imaging gonio-photometers*) or move the sensor around the sample (*scanning gonio-photometers*).

Scanning gonio-photometers offer advantages from a physics point-of-view: e.g. angular resolution, angular coverage, no relaying optics, isotropic sensor response, dynamic range and spectral resolution. But they had been prone to slow measurement speed, up to rendering them de-facto impractical for batch processing or routine checks in some applications.

A new design of a scanning, out-of-plane gonio-photometer is presented with optimised mechanical and electronic design, reduced scanning time, optimised sensors resulting in high dynamic range, low noise and extended measurement capabilities (e.g. VIS,IR,UV and polarisation).

Sample data and validation checks illustrate that this measurement design offers advantages and flexibility over previous concepts.

**Keywords:** BRTF, BSDF, gonio-photometer, scattering, stray light, illumination engineering, optical metrology

## 1. INTRODUCTION

Generally, scattering of electromagnetic radiation by matter is defined as relative power scattered into a small solid angle by a small volume of scattering material as a function of scattering direction, wavelength and polarisation. Applications range from sub-micron surface analysis to atmospheric effects.

The *bidirectional-reflection-transmission-function* (BRTF) defines scattering within the framework of geometrical optics and using photometric quantities for an infinitesimal surface element as:[2]

$$\mathcal{L}_{out}(\vec{x}_{out}) = \int_{\vec{x}_{in}}^{\Omega_{in}=4\pi} BRTF(\vec{x}_{out}, \vec{x}_{in})\ \mathcal{L}_{in}(\vec{x}_{in})\ \cos(\alpha_{in})\ d\Omega_{in} \tag{1}$$

Where $\mathcal{L}_{in}$ is in incident radiance on a surface element from a direction $\vec{x}_{in}$, $\mathcal{L}_{out}$ is the outgoing radiance from this surface element into a direction $\vec{x}_{out}$, $d\Omega_{in}$ is a infinitesimal solid angle around $\vec{x}_{in}$ and $\alpha_{in}$ is the angle between the surface normal and $\vec{x}_{in}$.[3] * The cos-term in (1) is cosmetic and causes the BRTF being formally constant for so called *Lambert*-emitting scattering surfaces. To facilitate display, handling and processing, a definition $BRTFc := BRTF \cos(\theta_{out})$ is introduced and used in this text for plots.

Further author information:
email techsup@pab.eu, website www.pab.eu

*This quantity is also known as BSDF (*bidirectional-scatter-data-function*), BRTDF (*bidirectional-transmission-reflection-distribution-function*), BRTD (*bidirectional-transmission-reflection-distribution*), depending on author's preference and to discriminate between measured data and fitted functional model, or between reflection and transmission.

From definition (1) follows that the BRTF depends on 4 angles for the two directions, with the BRTF optionally depending additionally on wavelength $\lambda$, position on the sample, polarisation, time and other parameters. In this text, a direction $\vec{x}$ is described by a coordinate pair $(\theta, \phi)$ of a classical polar coordinate system: [†] Writing $BRTF(\theta_{in}, \phi_{in}, \theta_{out}, \phi_{out})$, a specific, user defined direction on the sample defines $\phi = 0^o$, and $\theta_{in} = 0^o$ defines the front surface of the sample. For example, with incident light on the front surface ($\theta_{in} \in [0, 90^o]$), $\theta_{out} \in [0, 90^o]$ describes reflection, $\theta_{out} \in ]90^o, 180^o]$ transmission. For some 2D plots, a negative $\theta_{out}$ value is equivalent to $(|\theta_{out}|, \phi_{out} + 180^o)$. Vector $\vec{x}_{in}$ and surface normal $\vec{n}$ span the *scattering plane*.

This implicit definition of BRTF is mathematically robust and contains all possible cases, including the BRTF of "void", which is written using the *Dirac delta function* [‡] $BRTF = \delta(\vec{x}_{out} - \vec{x}_{in})/\cos(\alpha_{in})$, leading to $\mathcal{L}_{out} = \mathcal{L}_{in}$. Since materials with high transmission or reflection and low scattering approach this abstract $\delta$-function, this is relevant in practice:
Any measurement of the BRTF is necessarily an average of the "true" BRTF over finite angles $\Omega_{in}$ (solid angle subtended by lamp as seen from sample) and $\Omega_{out}$ (solid angle of detector). For samples with low scattering, whose therefor "peak"-like BRTF structure is non-zero in a smaller angular area then $\Omega_{in}$ or $\Omega_{out}$, the measured numbers will depend on machine-specific $\Omega_{in}$ and $\Omega_{out}$ (see example in section 3.3.3).

Datasets resulting from the optimised device described here[§] are typically asymmetric in resolution for incident and outgoing angles: $BRTF(\theta^i_{in}, \phi^j_{in}, \theta^k_{out}, \phi^l_{out})$ described are a sparsely filled matrices, with only a few $\theta_{in}, \phi_{in}$ values and around 100000 measured samples $(\theta^k_{out}, \phi^l_{out})$ per incident direction. (see section 2.2). The reason is an adaptive measurement strategy that describes the BRTF more compact:

Measuring the BRTF for a fixed incident angle means sampling an unknown function of two variables $(\theta_{out}, \phi_{out})$. Sampling frequency corresponds to spatial sampling density of $(\theta_{out}, \phi_{out})$ in this case, and the usual sampling and aliasing laws apply:
Smooth BRTFs (semi-glossy or matt surfaces ) require little thought on sampling frequency and aliasing, since their highest frequency in variables $(\theta_{out}, \phi_{out})$ is low. BRTFs with higher frequency show localised peaks, which have to be sampled adequately. However, from a practical standpoint, these materials have the most useful applications (light redirection, controlled asymmetric diffusion, etc) making BRTFs with peak- or ridge-shaped structures in $(\theta_{out}, \phi_{out})$ the most interesting to measure. [¶]
As with any aliasing problem, there are two ways to avoid under-sampling and artifacts: Increase sampling frequency above the Nyquist minimum or pre-filter the signal to lower the maximum frequency in the signal. In the first way the BRTF is sampled with a fixed high resolution (see section 2.2.2), which is a robust way with an increase in measurement time. In the second way the detector area and thereby its solid angle is increased to be larger than the angular distance between coarse sampling points, which is also robust, but limits angular resolution to the point that resolution of peaks is not sufficient.
A third way samples the BRTF in multiple steps, first with a low sampling frequency and then with a higher sampling frequency in selected areas. This adaptive methods limits the potentially time consuming high resolution to areas of interest, while keeping measurement time to a reasonable minimum. However, it requires that either the areas of interest are known in advance by the user, or are located automatically by algorithms after a pre-scan ([4]). One of the core capabilities of the pgII is to offer all three methods and leave the choice to the user, depending on site requirements.

A high dynamic range of detector allows measuring the beam without sample as reference, providing absolute BRTF measurements without using external reference samples. The dynamic range and opening angle of the detector limit the lowest measurable BRTF.

Further BRTF processing include visualisation, mostly 3D plots for each $\theta_{in}, \phi_{in}$ or 2D plots of data in the scattering plane. Visualisation of data before further processing proofed to be an effective concept for cross-checks of results.

---

[†] Angular units are given in degrees, unless noted otherwise.

[‡] Sometimes referred to as *Kronecker delta function*: $\delta(x) = \{\, 0 \,\forall x \neq 0\,,\, \infty \, for \, x = 0\}$, with: $f(0) = \int \delta(x) f(x) dx$ .

[§] model *pgII*, revision B

[¶] Varying $(\theta_{in}, \phi_{in})$ results in relatively smooth changes in topology of the BRTF for $(\theta_{out}, \phi_{out})$, allowing a coarse sampling of the incident direction.

The applications of BRTF measurement determine priorities of measurement details, all covered by the pgII, which can be roughly categorised as:

- stray light analysis in imaging optics generated interest in scatter measurements, dating back to around 1970 (see overview[5]). This continues to be of interest and implies BRTF measurements with high angular resolution, small opening angles of detector and source (small *instrument signature*), with emphasis on angles around the forward or ideal-specular direction. In this context the BRTF is regarded as something to be minimised (approaching the ideal $\delta$-function) in order to minimise stray light.
- light redirection, e.g. using architectural glazings for daylighting,[6,7] is using complex materials (e.g. holografic) and structures to alter the direction or shape of light beams. The BRTF is of interest on the whole sphere, not just around the forward or specular peaks and is actively shaping light distributions. This includes uses of measured BRTF in illumination optics, especially in combination of simulation: beam shaping of laser diodes, white LEDs and window materials for day-lighting among the uses. Angular coverage and measurement time become more prominent, while the dynamic range remains a primary requirement in any case.
- material research is using BRTF data for models of surface roughness (RMS) and surface treatment. This application requires parameters of gonio-photometers between imaging optics and illumination optics applications, with possible extensions to polarisation and wavelength.

## 2. CONCEPT AND GENERAL LAYOUT

### 2.1 mechanical

#### 2.1.1 possible configurations

The three components of a Gonio-Photometer for passive[‖] materials are light source, sample mount and detector. They can be arranged in different geometrical ways, with the number of light sources, orientation of rotational axis for sample mount and the number of detectors as primary parameters. Angular coverage of incident and outgoing angles, angular solid angle of the light sources and detectors , spot size of the beam at the sample and spectral range are among the secondary parameters.
Some setups measure the BRTF in the scattering plane only,[8] however, data for the out-of-plane angles is missing and can only be extrapolated in limited cases using further assumptions and models on the angular distribution.
Imaging gonio-photometers use at their core a planar position-resolving sensor (CCD or CMOS image sensor) and optics (screens, or domes and lenses) to map a position on the chip to an outgoing direction as seen from the sample[7,9] . The high-speed readout speed of commercial of-the-shelf image sensors results in very fast simultaneous capture of a fixed set of outgoing directions. Inherent drawbacks include the limits of available sensors (dynamic range, spectral range, homogeneous response) and limits within the optical relay system (added stray light, lens errors, spectral range).
Mechanical scanning systems consist of one or more detectors whose mechanical positions are located on a surface around the sample. Speed and precision are the main parameters of the mechanical support systems. Various machines built during European and international research programs have featured various designs[10–14] .

#### 2.1.2 pgII layout

Conceptual, the pgII is a gonio-photometer with a mechanical scanning system, with two computer-controlled sample-axis and a two axis controlled, out-of-plane, sensor head carrying multiple sensors. Industrial drive systems, as used in robotics, drive the freely rotating sample and fast detector arm. It is based on an earlier (1990) gonio-photometer by the author, which used a different and more limited mechanical configuration.[12]
To shorten measurement time, measurement are done continuously, while moving (on-the-fly) and the motion system allows arbitrary continuous movement of the detector head on the sphere. This allows optimised scan patterns, explained in the following sections.
As a side-effect, this concept allows a variety of intrinsic cross-checks and self-tests which are used to verify the integrity of measured data without requiring external references. This is detailed in section 4.2.

[‖] Gonio-Photometers used for measuring lamps are a different category.

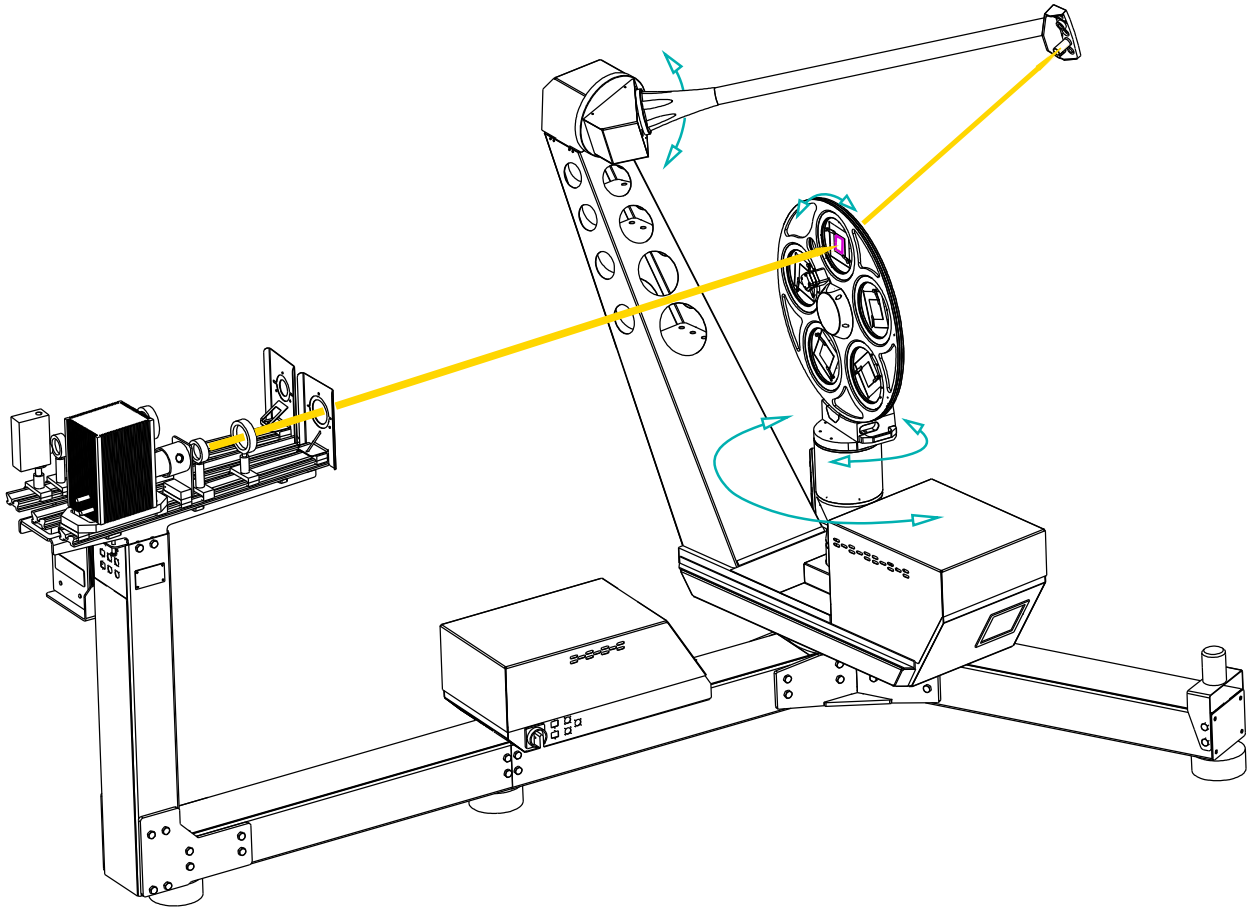

Figure 1. isometric view of the pgII gonio-photometer, with indicated directions of incident and scattered light. The arrows indicate rotational axis of detector and sample mounts. Drawing shows the optional automatic sample changer.

## 2.2 measurement strategies

### 2.2.1 coordinate system at the sample and data display

A classical polar coordinate system is attached at the sample: $\theta = 0^o$ along the positive Z-axis of a right handed Cartesian coordinate system, $\theta = 90^o$ in the XY-plane and $\phi = 0^o$ along the positive X-axis. The incident direction is defined as the direction towards the lamp. For example, the ideal specular reflected peak is at ($\theta_{in}$, $\phi_{in} + 180^o$), the unscattered forward peak at ($180^o - \theta_{in}$, $\phi_{in} + 180^o$).
For visualisation, one hemisphere is projected onto the XY-plane, $\theta_{out} = 0^o$ (reflection if $\theta_{in} < 90^o$) or $\theta_{out} = 180^o$ (transmission) at the centre, $\theta$ increasing (or decreasing in the case of transmission) linearly towards $\theta = 90^o$ at the edge of the disc, $\phi$ plotted circular around the centre and the signal linearly or logarithmic above the plane (fig. 2 and 3). For $\theta_{in} > 90^o$ the reflection/transmission notation is reversed accordingly.

### 2.2.2 path generation

Measurement points are located along the paths of the detector sensors, with mechanical speed and fixed sampling frequency determining their angular spacing along the path. Modular software blocks, *path generators*, provide path types that cover regions of the sphere that are to be measured. This provides a flexible, modular and extensible way to measure complex patterns in the BRTF with a trade-off between angular resolution and measurement time: For example, *fullrot* paths covers background scattering with speed and spacing between neighbouring lines as user selected parameters. *inplane* paths cover a area above and below the scattering plane. And *spiral* paths are used to resolve peaks in the BRTF. Fig. 3 and Fig.4 show examples.

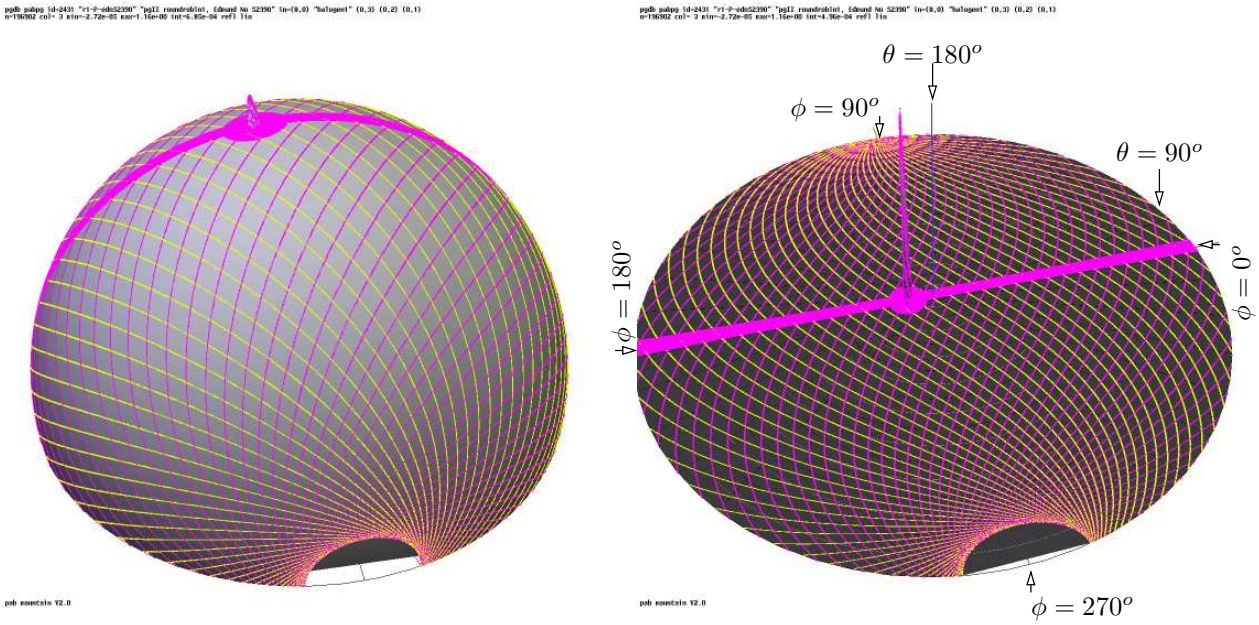


Figure 2. Scan paths on the transmission hemisphere: Left image shows *fullrot*, *peak* and *inplane* paths. Right image shows the hemisphere projected onto a plane, with detector signal linearly as height over the ground plane.

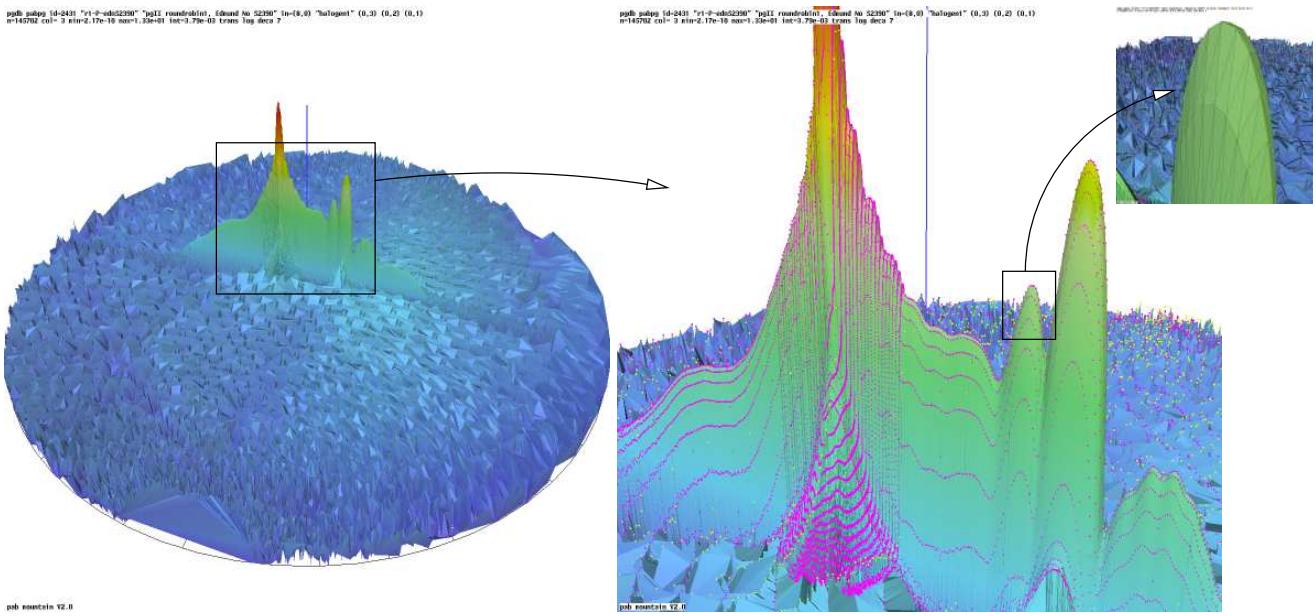

Figure 3. Data visualisation of measurement whose paths are shown in fig 2: Left image shows the complete dataset (145702 data-points) of the transmission of a 3M "micro-louvre" film for ($\theta_{in} = 8^0, \phi_{in} = 0^o$) using a logarithmic Z-scale. Right image shows a close up of the peak region. The insert displays the triangulation used for display and interpolation. Note the finer structure of the BRTF "ridge" resolved by *inplane* and *spiral* paths.

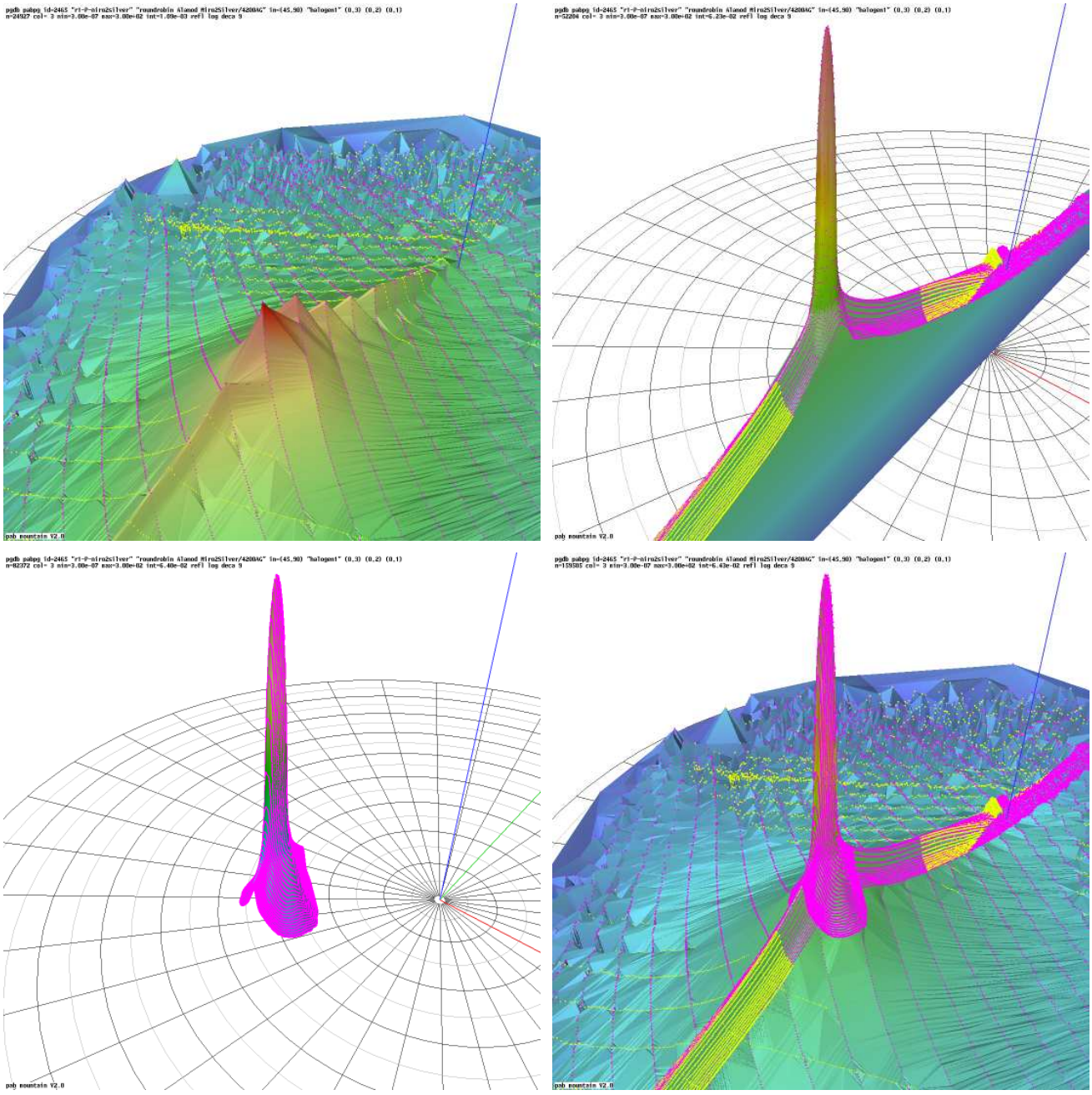

Figure 4. measurement of a BRTFc with peak and ridge structure, combining different scan methods:
Top left: *fullrot* method covers the while sphere quickly, supplies data on the diffuse low-level scattering and shows aliasing around the peaks and ridge due to insufficient resolution (24928 data points).
Top right: *inplane* method resolves to ridge along the scattering plane and covers the peak (52205 data points)
Lower left: *peak* method resolves the peak in more detail (91337 data points).
Lower right: complete dataset of all methods combined (logarithmic z-scale for all plots: $[3^{-7} : 3^{2}]$)

### 2.3 detector subsystem

To achieve reproducible measurements on-the-fly, the detector system spans a wide dynamic range of more then 6 decades and the synchronisation between optical signal and mechanical position is fast and stable (see 4.2).

The currently used detectors operate in photo-voltaic mode using different sensor materials ** and a compact custom developed board for amplifier and analog/digital conversion directly at the detector head. This results in low noise, high dynamic range with a standard data rate of 1kHz as shown in fig. 15. Each sensor is equipped with a tube and baffle system to shade the sensor area from stray light and limit its angular acceptance (field of view) to the sample area. The detector head is built modular to support multiple sensors and the electronics allows sensors to be read out in parallel, shortening measurement time.

Using identical sensors with different pre-amp settings acquires the full dynamic range with one mechanical scan. Alternatively, different filter or sensor combinations captured the BRTF in spectral bands or for different polarisation states.

### 2.4 lamp subsystem

In the standard configuration, light sources are mounted on horizontal optical benches 2.2m from the sample, with a current maximum of three rails aiming at the sample centre. Sources are software controlled, either by switching the power supply or a shutter (Xenon lamp). This allows automatic monitoring of warm-up period and lifetime statistics. An extra sensor at the lamp itself is optional, but not imperative in practice. Problems with instabilities of the Xenon arc from previous gonio-photometers[4] have been overcome by component manufacturers, notably in details of the Xenon bulb and power electronics, making an explicit reference sensor for the beam redundant. Polychromatic light sources (Xenon- or Halogen-lamps) use the classical filtering by a condensor, pinhole and lens, focusing the pinhole either on the sample or the detector.[3] The differences are spot size diameter at the sample and angular resolution. Optional filters shape the overall spectral response (see fig. 16). Fig. 5 plots cross sections of different beams.

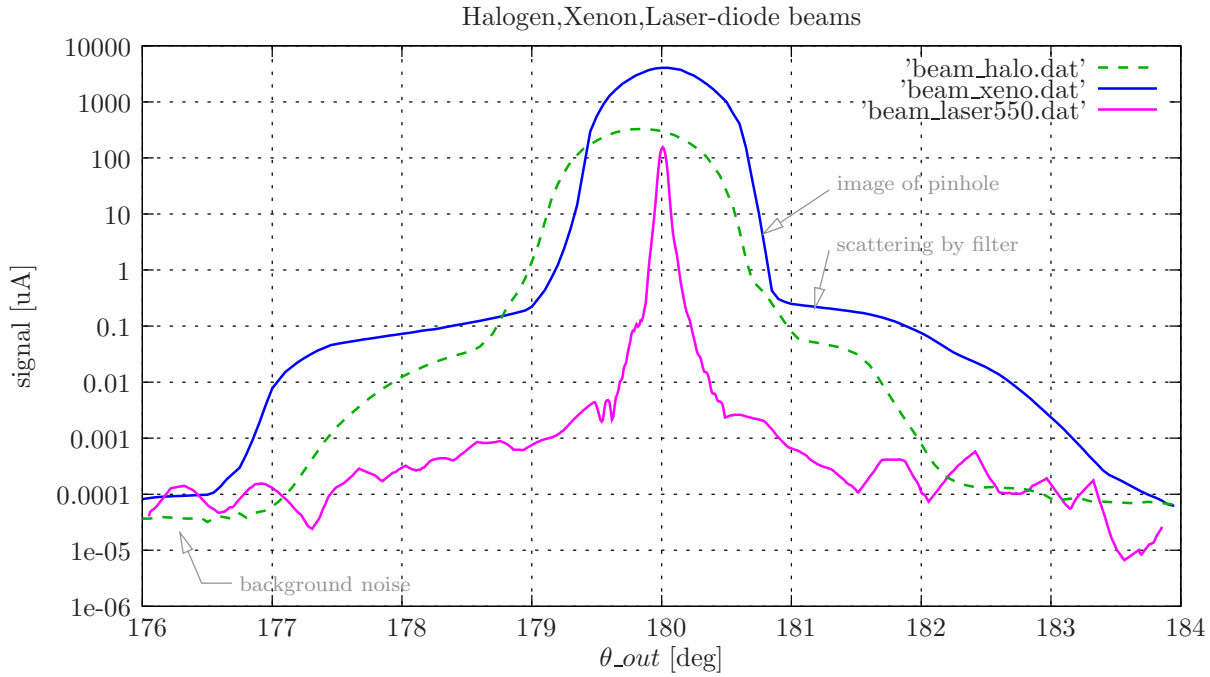


Figure 5. cross-sections through beam-profiles of Xenon, Halogen and laser-diode light sources.

**Other detector types are possible, with the restriction that their operation should not dependent on orientation (e.g. excluding most Dewar-type cryogenically cooled IR sensors), be fast (most mid-IR sensor would slow down the measurement speed considerably) and mechanically stable.

## 3. EXAMPLES OF MEASURED BRTF

### 3.1 narrowly diffusing BRTF of rolled aluminium

As an example of reflective scattering material, fig. 6 shows the BRTF of *Miro 20/2000 GP* coated aluminium is shown. The aluminium is rolled to thinner sheets ("coils") during manufacturing and this roll-direction causes an asymmetric BRTF, even after further coating. Fig. 7 plots cross-sections through the dataset for different incident angles. It also displays results for two lamp system as a validation step.

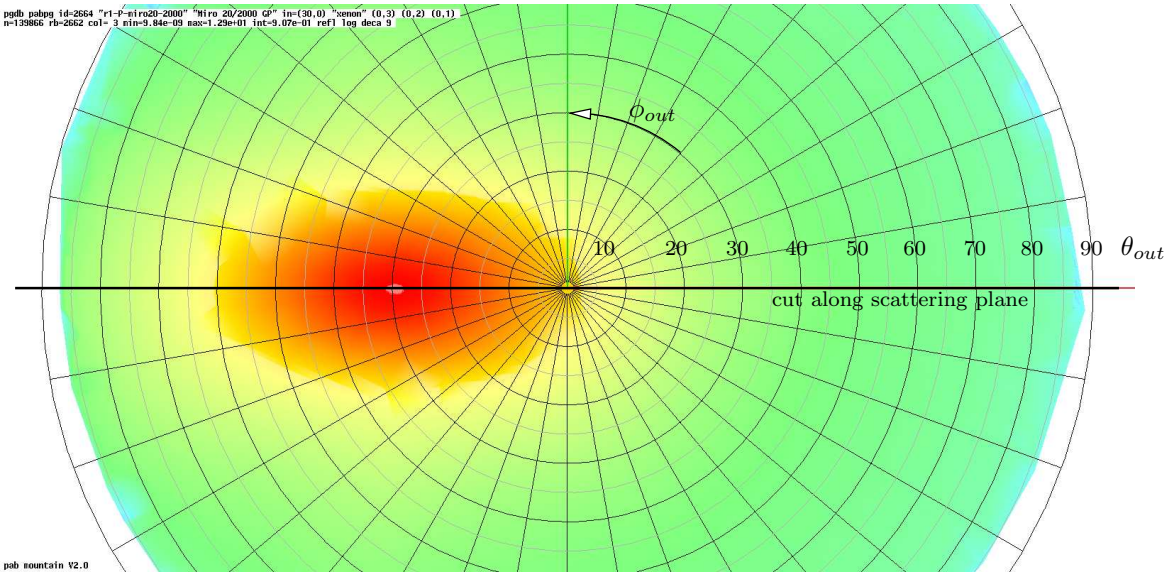


Figure 6. False-colour plot of BRTFc of Aluminium surface for $\theta_{in} = 30^o$, showing asymmetric scattering.

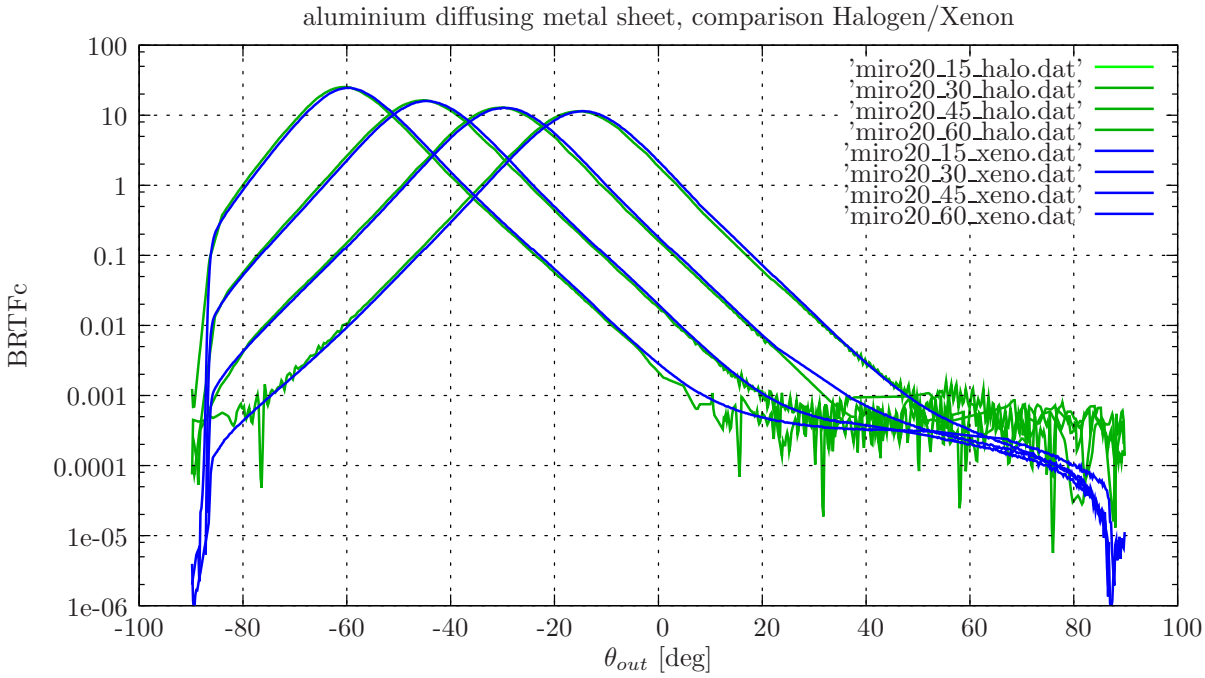


Figure 7. Aluminium surface BRTFc cross-section ($\phi_{out} = 0^o$) of dataset of fig. 6, incident angles $\theta_{in} = 15, 30, 45, 60^o$

### 3.2 near-Lambert constant BRTF of PTFE

PTFE (poly-tetra-fluor-ethylene, commonly known as *Teflon*$^{\mathrm{TM}}$) is used for the inside of integrating spheres, where it is assumed to be ideal diffusing (constant BRTF). As an example, fig. 8 shows a false-colour polar plot of the reflected BRTF: One surface is face-milled, which introduces an asymmetric pattern on the surface (middle image), the other surface was milled and ground, resulting in a stochastic surface with symmetric scattering.

BRTF of two PTFE samples is plotted in fig. 8: Samples had been made from the same batch (15mm thick): "raw" has a cleaned, but otherwise unchanged surface after manufacturing, the "80" surface had been front-milled and ground. The Y-axis in fig. 8 plots the deviation from an ideal reflecting and constant BRTF ($\rho_{dh} = 1$) in percent. The processed surface proofs an error less than 5% up to $\theta_{out} = 80^o$ for $\theta_{in} = 35^o$, but still forward scattering for $\theta_{in} = 60^o$. For the unprocessed "raw" surface this forward scattering is 4-times larger.

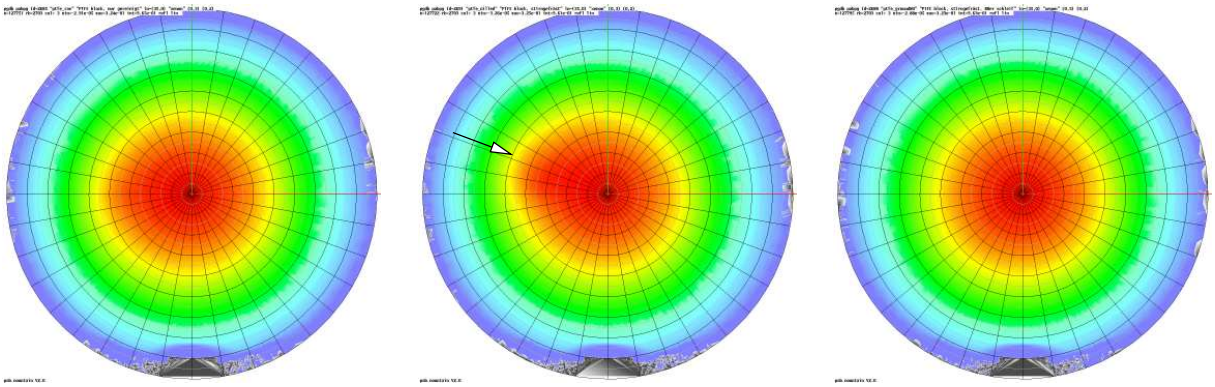

Figure 8. false-colour image of BRTFc for three PTFE samples, $\theta_{in} = 35^o$. Left: raw PTFE, middle: milled surface with asymmetry (marked by arrow, see text), right: symmetric dataset of milled and ground sample.

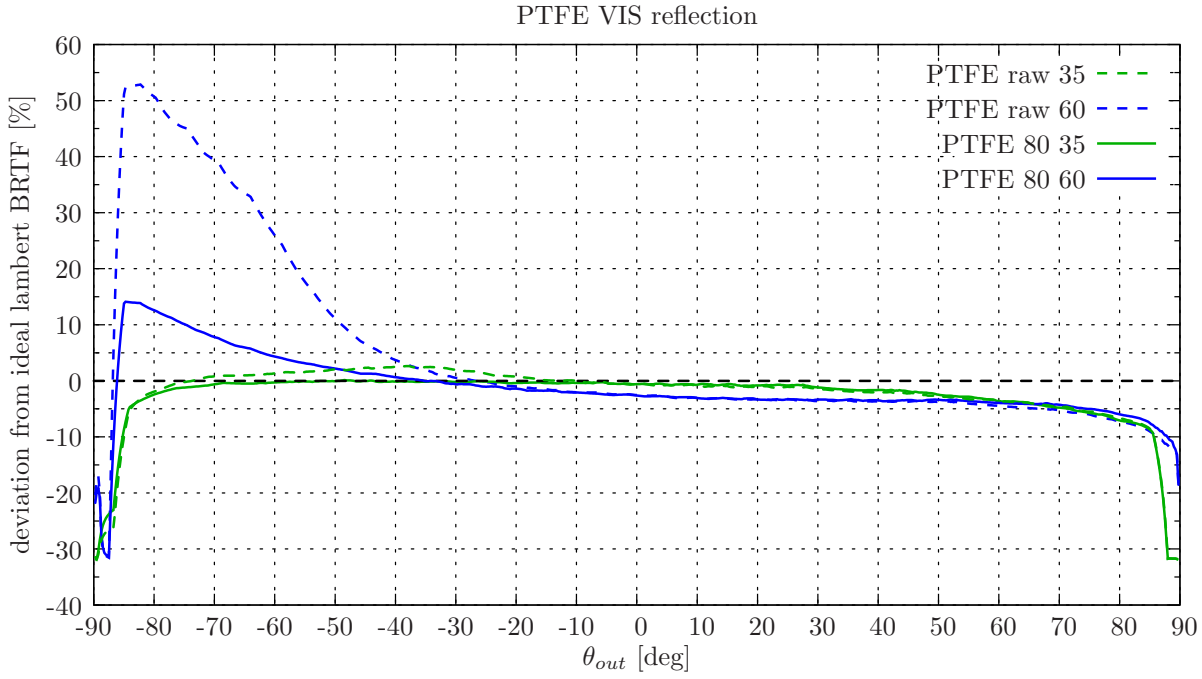


Figure 9. 2D cross-section of BRTF deviation from ideal lambertian of two PTFE samples for $\theta_{in} = 35, 60^o$, for raw and milled+ground surface. Note increase in specular reflection for higher incidence angles.

### 3.3 BRTF of prism

An equilateral prism serves as a just-above-trivial example with well known properties to validate angular accuracy of peaks for a sample with low optical scattering. As a side effect, the setup may directly indicate the overall spectral response of the lamp-detector system when used with a polychromatic light source. Rays in this prism are sketched in fig. 10. [††] Fig.11 shows the BRTF in the scattering plane.

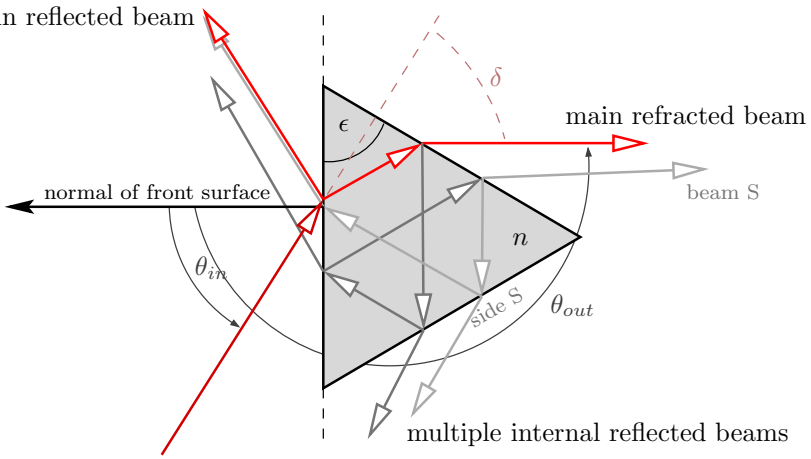


Figure 10. Raytraced reflected and refracted beams in an equilateral prism of refractive index $n$

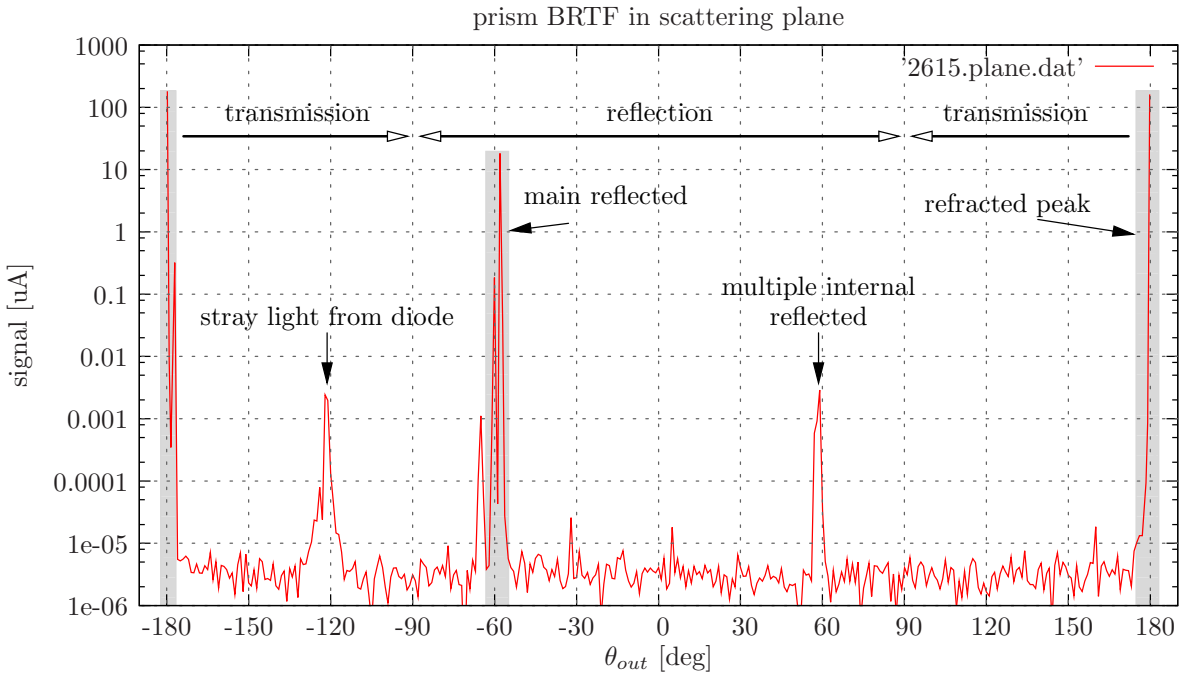


Figure 11. BRTF data of prism in scattering plane for $\theta_{in} = 57, 68^o$. $\theta_{out}$ is defined as in Fig. 10, with negative values corresponding to directions $\phi_{out} = 180^o$ in polar coordinates. The X-axis wraps around from -180 to +180. Finely resolved datasets of refracted and reflected main peaks (shaded areas) are given in fig. 12 and fig. 13. Note the smaller peaks fig.11 next to refracted and reflected peaks due to multiple internal reflections as shown in Fig. 10.

[††]Beams in prisms are peculiarly more interesting than in most textbooks: Note that beam S gets refracted but not dispersed, since the three internal reflections reverse orientation. Linear polarisation of S is higher then the main beam.

### 3.3.1 Details of data and prism

The prism (dimensions 30x30x30 [mm], EdmundOptics No 43497) is mounted on a small horizontal optical table at the centre of the pgII. One of the three sides was chosen as front surface and aligned collinear with the vertical pgII sample rotational axis. This surface was oriented to retroreflect the incident beam for $\theta_{in} = 0^o$. Thereby the incident angle $\theta_{in}$ that is used within the pgII terminology is identical with the incident angle for prisms in classical text books.[15, 16]

To achieve the desired angular resolution, a 1mm pinhole was added at the Si detector and a laser diode was chosen as light source. The refracted peak and the reflected peak off the front surface where scanned at high angular resolution, while the a band above and below the scattering plane was scanned at medium resolution. Fig.12 shows a close view of the high resolution sampling of the refracted peak. Measurement path is a zig-zag up-down movement of armB while armA is moving continuously.

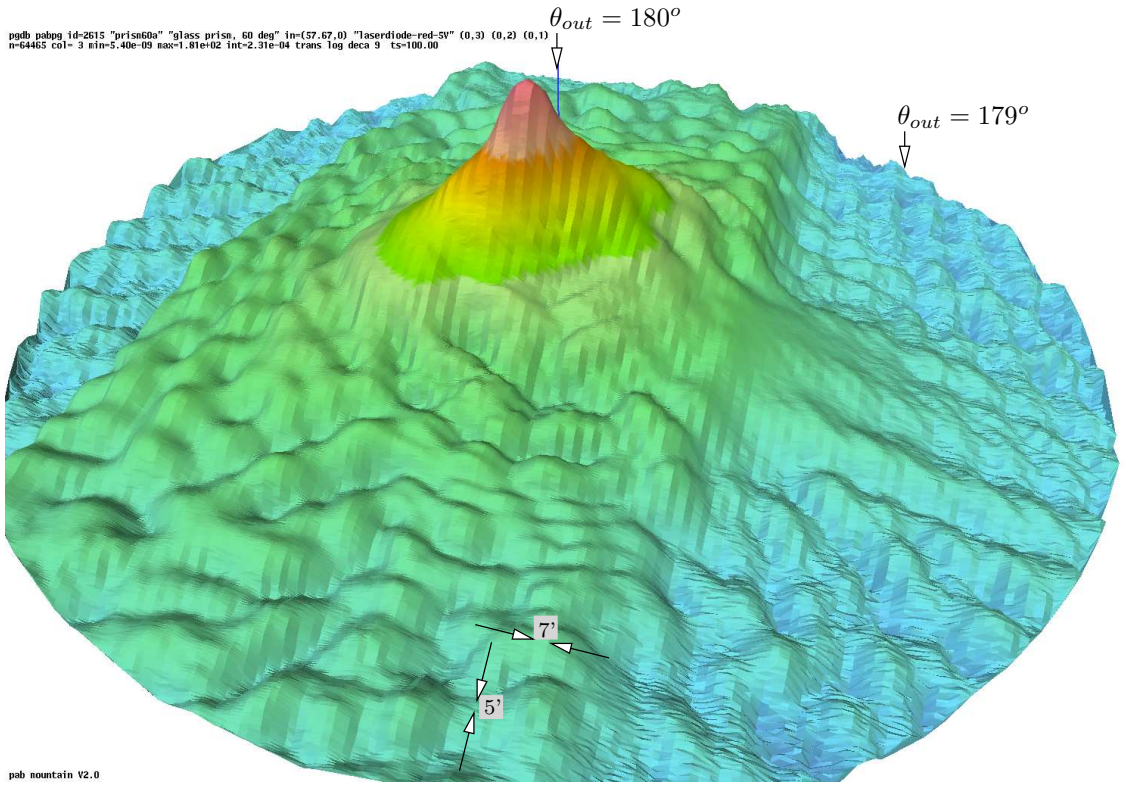


Figure 12. Enlarge area around refracted peak for $\theta_{in} = 57,68^o$, using a laser diode at 650nm and a 1mm detector pinhole. Plotted are 64465 data-points for $\theta_{out} > 179^o$ with a spatial resolution of 7' by 5' . Maximum signal at peak is $1.8 \cdot 10^2$, minimum in "valleys" is $4 \cdot 10^{-5}$ [uA].
The rectangular area around the peak is caused by stray light of the laser diode reflected in the prism and its interference patterns. Outside this elevated signal additional stray light is generated by the prism itself.

Fig. 13 shows cross sections through the main refracted peak and the main reflected peak, for a set of $\theta_{in}$: 57.6 , 57.68 , 57.7, 57.8 degrees. Clearly, an angular resolution below $0.1^o$ is achievable for both outgoing and incident directions. The wave pattern for low values is due to the interference patterns also shown in fig. 12.

### 3.3.2 Calculating $n$ of prism material

One use of prism spectrometers is to get the index of refraction $n$ from $\delta$. For this, $\theta_{in}$ was adjusted to put the outgoing beam at $\theta_{out} = 180^o$. Than $n$ is given by $n = \sqrt{(1 + \cot\epsilon \ \sin\theta_{in})^2 + \sin\theta_{in}^2}$ with $\epsilon = 60^o$ for this equilateral prism. Reading from fig. 13, a value of $\theta_{in} = 57.68^o \pm 0.02^o$ seems a reasonable estimate. From above equation, an estimate for $n$ of 1.7113 can be concluded. Wavelength of the laser diode in use is specified by the

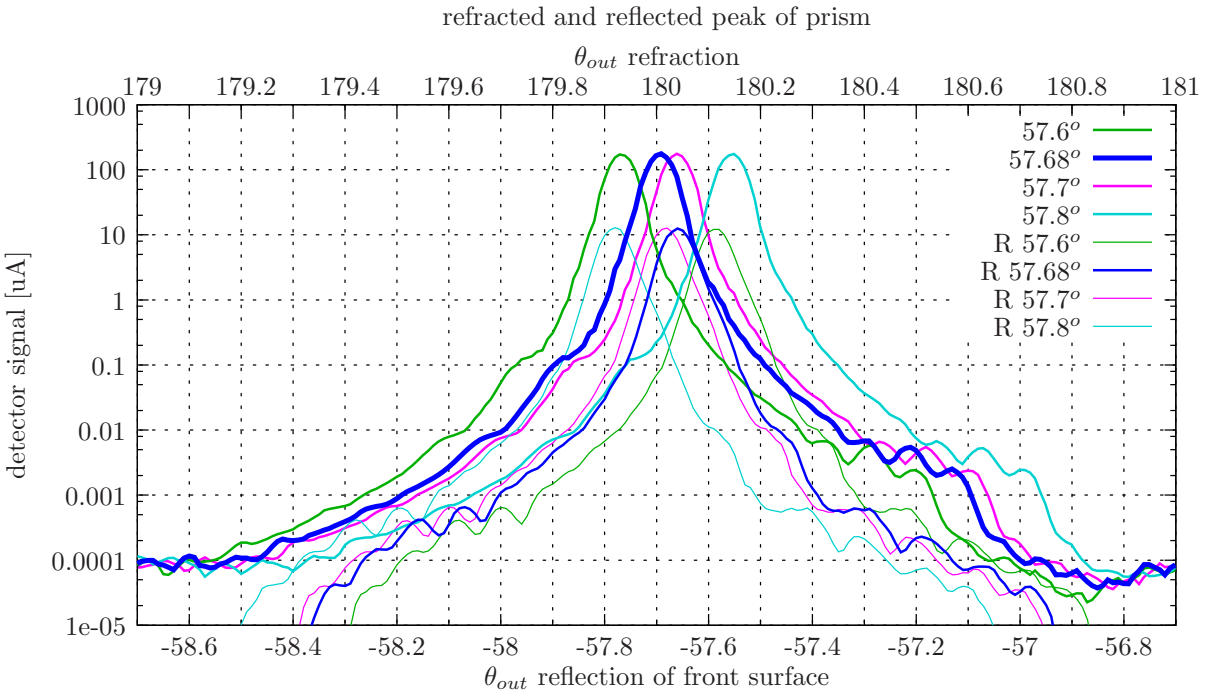


Figure 13. Details of refracted and reflected peaks shown in fig. 11 and 12. For three values of $\theta_{in}$ with a step size of 0.1deg and 57.68$^o$ . Curves for the refracted beam are higher and use the upper X-axis, curves for the reflection are lower and use the lower (reversed) X-axis.

manufacturer as $\lambda = 650nm$ . In comparison, data from Schott as glass manufacturer for the material of the prism, SF18, indicates a higher $n$ for 650nm, approx 1.715. If this is due to the laser diode emitting at a longer wavelength can be a subject of further investigation. A second test using a laser-diode at 532m, resulted in $\theta_{in} = 59.17^o$, n=1.747, with a tabulated value of 1.730. Results don't match published values for $n$ very nicely, however the specified material SF18 is not produced by Schott anymore. Since deviations are outside the error estimates of the pgII , there are doubts left as to the exact material used in manufacturing this prism.

### 3.3.3 Comparison of detector solid angles, *noise-equivalent-BRTF*

Data in fig. 11 was measured using a detector of square 10mm x 10mm surface with a 1mm circular baffle mounted in front ot it, using a very high angular scan resolution for two peaks as shown in the detailed plot fig. 13. Using the same detector with a 14mm circular baffle increases the signal by a factor of 100, as expected, and the detector signals of the two datasets are compared in fig. 14.

The BRTF of the prism features peaks which are narrower than the angular resolution of the detector with the 14mm baffle. The comparison therefor exemplifies the principal problems in this case: In fig. 14, the two peak regions A show a higher detector signal since the 1mm pinhole was smaller than the peak width. Regions B show more detail in background stray light, which was below noise levels for the smaller baffle. Region C shows a different structure of the peak, indicating and confirming that the angular scan resolution for the 1mm pinhole was not high enough to resolve the true location and height of the peak at $\theta_{out} = 60^o$, which was of no concern for the prism measurements and therefore deliberately not scanned finely.

Dividing the detector signals by the measured and integrated unobstructed beam for each detector baffle is shown in fig.15. Smaller detector opening angles result in higher BRTF values, while the noise-equivalent BRTF[17] is lower with the larger detector surface (see also fig. 7). Both effects are expected from theory of BRTF measurements and confirm integrity of the pgII measurements. Beam profiles are shown in fig.5.

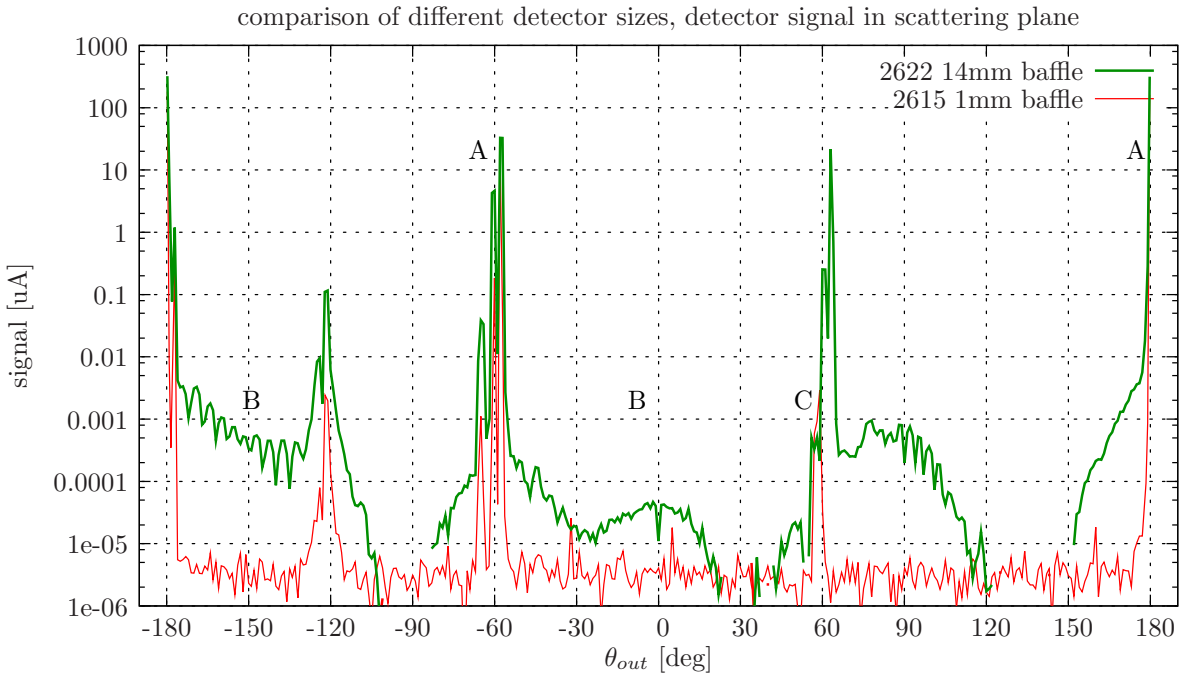


Figure 14. Same data as in fig. 11, using a 1mm detector baffle, compared to same set up using a 14mm detector baffle.

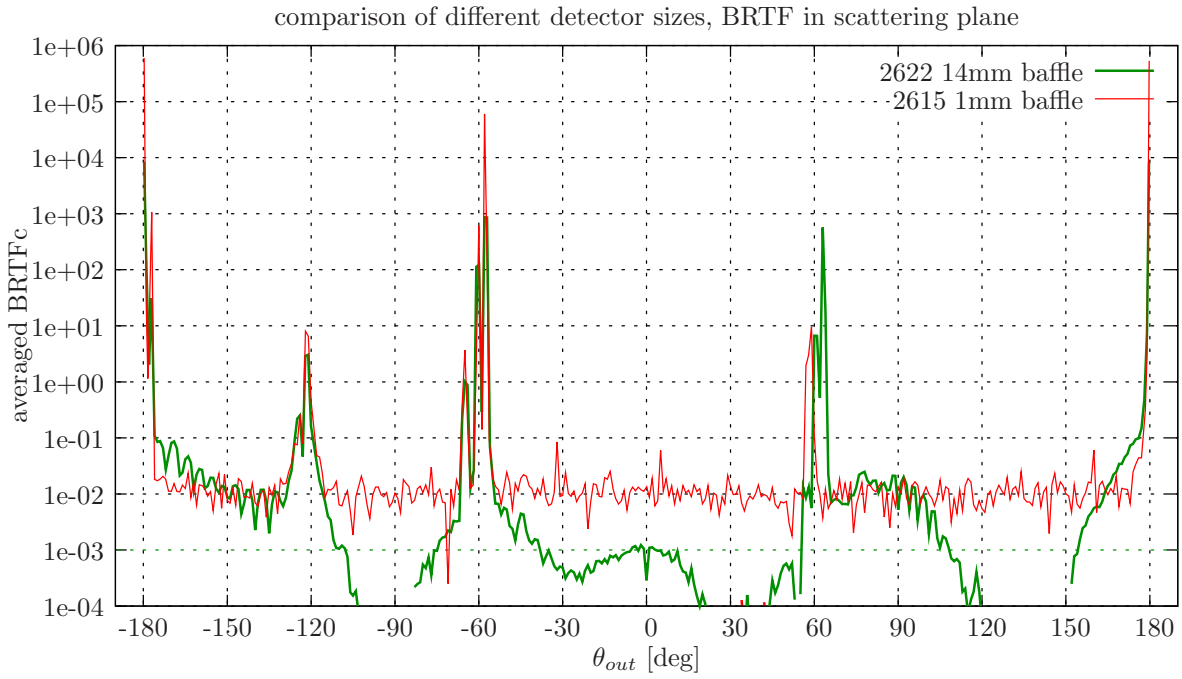


Figure 15. Comparison of measured prism BRTFc using two detector sizes. Same data as fig. 14, but detector signal is divided by the integrated reference beam for each detector size.

### 3.3.4 Polychromatic light sources

Generally the wavelength dependent response of the pgII is the product of emitting spectra of the lamp, filtering by optical components along the lamp setup, transmission- and reflection spectra of the sample, optional filters in front of the detector and response of the detector material. Even crude knowledge of the response is helpful, for example in comparing BRTF measurements with integration spheres or other gonio-photometers, which may have a different response. Especially using Silicon as detector material together with incandescent light sources tend to shift the peak of overall spectral response towards the near IR. This may cause results of some materials, notably plastics in day-lighting-applications, to be significantly different from measurements done with equipment having a $V(\lambda)$-response.

The overall wavelength dependent response may be estimated by numerically multiplying individual spectrums of components, if these are available from data-sheets or by external spectrometers. Alternatively, the detector response and source spectral distribution may each be measured by portable spectrometers and monochromators. Both methods require external data and extra equipment. Using the prism with a known refractive index curve $n(\lambda)$ offers a way to estimate the overall wavelength with an intrinsic measurement and no further external equipment or data.

Using a white light source instead of lasers results in a spectrum around the single refracted peak of fig. 11, indicating the spectral response of the combined system of light source and detector.

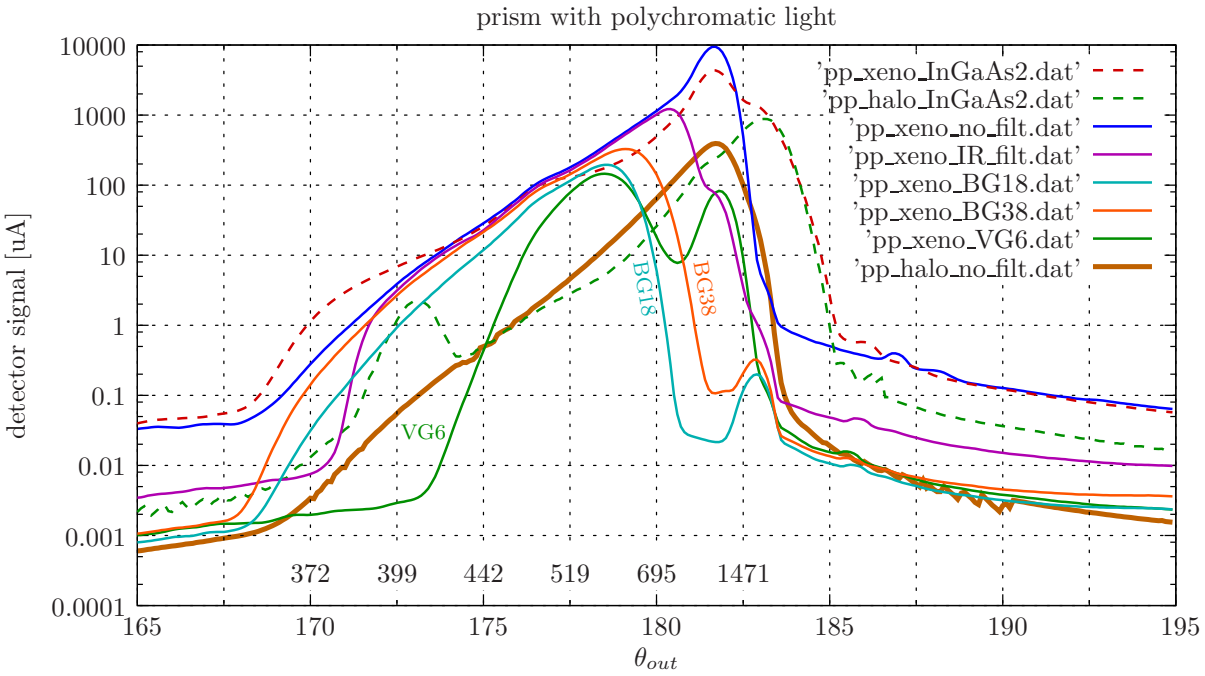


Figure 16. Cross-section of signal in scattering plane around refracted beam ($\theta_{in} = 57, 68^o$) . Dashed curves are for InGaAs detector with Xenon- or Halogen lamp. Other curves use an Silicon sensor, with Xenon or Halogen lamp ("no_filt") and Halogen with filters: 700nm IR edge filter and BG18, BG28 glass filters.
Numbers at bottom of plot are preliminary and correspond to wavelength in [nm], assuming a prism material SF18, which is uncertain (see text). The correlation is strongly non-linear, as usual for prisms.

### 3.4 BRTF of light redirecting micro-structure

As an example for materials with a non-standard BRTF, fig. 17 visualises datasets of a micro-structured material for light redirection in day-lighting applications. Above a threshold for the incident direction $\theta_{in}$, direct transmittance is blocked and light is redirected.

In an architectural installation, light is redirected towards the ceiling, illuminating the room while thereby blocking excessive direct light near the window. Fig. 17 illustrates this by the higher redirected peaks compared to the transmitted peak. Note that fig. 17 uses a log Z-scale.

The stray light (area in front of the "ridge" in fig. 17) is relevant for a day-lighting application, since may cause glare and discomfort to the inhabitants. The different colour in fig. 17 indicates a higher level of stray light for higher incident angles. Explaining the more detailed examination and application to day-lighting is beyond the scope of this paper.

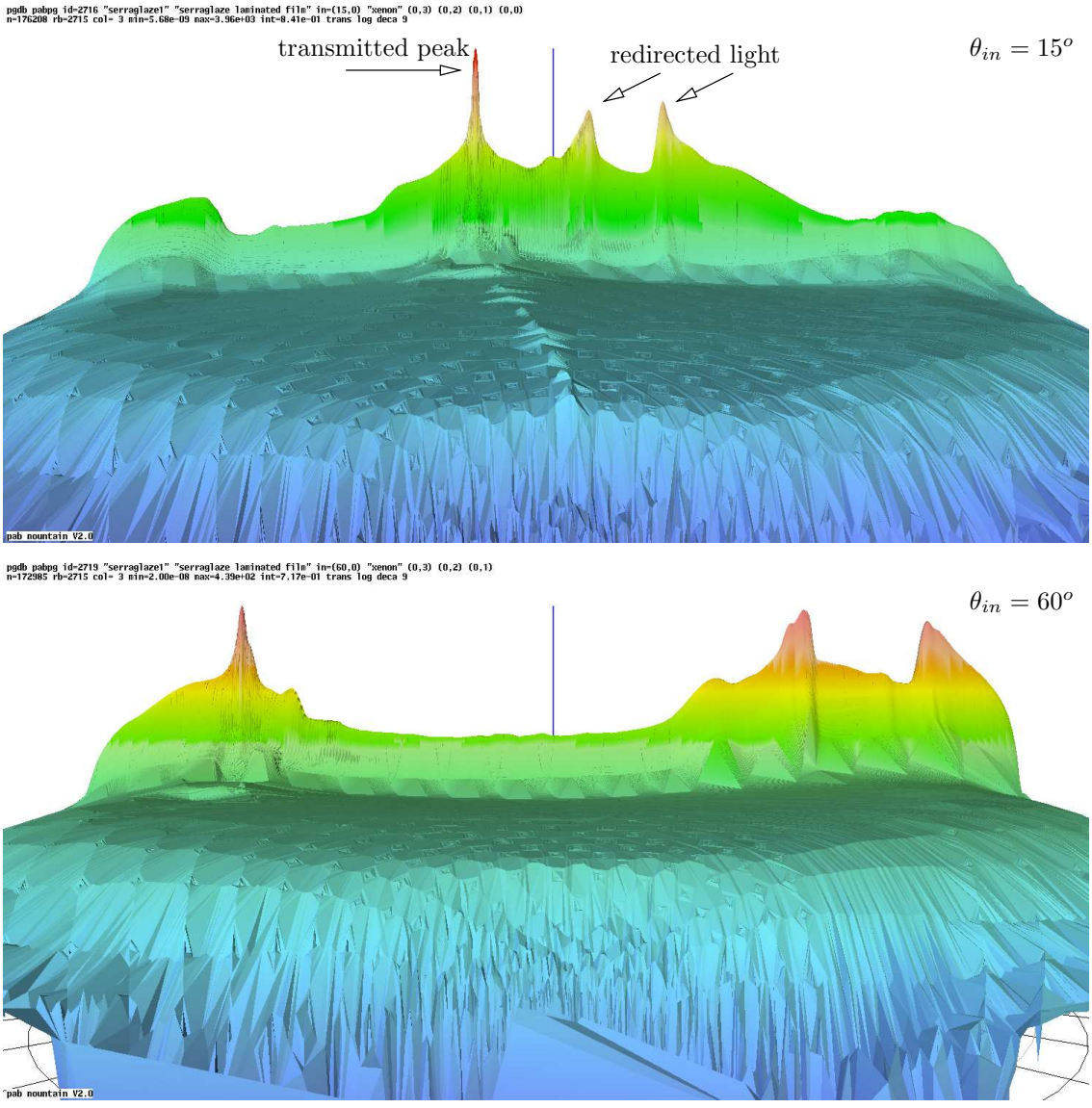


Figure 17. BRTFc of micro-structured material for $\theta_{in} = 15^o$ and $60^o$ . Z-axis scale is logarithmic, 8 decades.
Sample courtesy of BendingLight and De Montfort University, UK, Dr. Mardaljevic, 2008

### 3.5 BRTF of Silicon wafer in middle IR

Since Silicon is transparent between 1.5um and approx 6um, it serves as example for measurements using the InGaAs sensor, whose spectral maximum response is given by its manufacturer as between 1.8 and 2.4 [um].

It is worth to note that transmission of the three samples differ greatly (fig. 19): Two show a very pronounced forward peak with differ scattering around it. The third shows an almost ideal diffusing characteristic, which is nearly independent of the the incident direction.

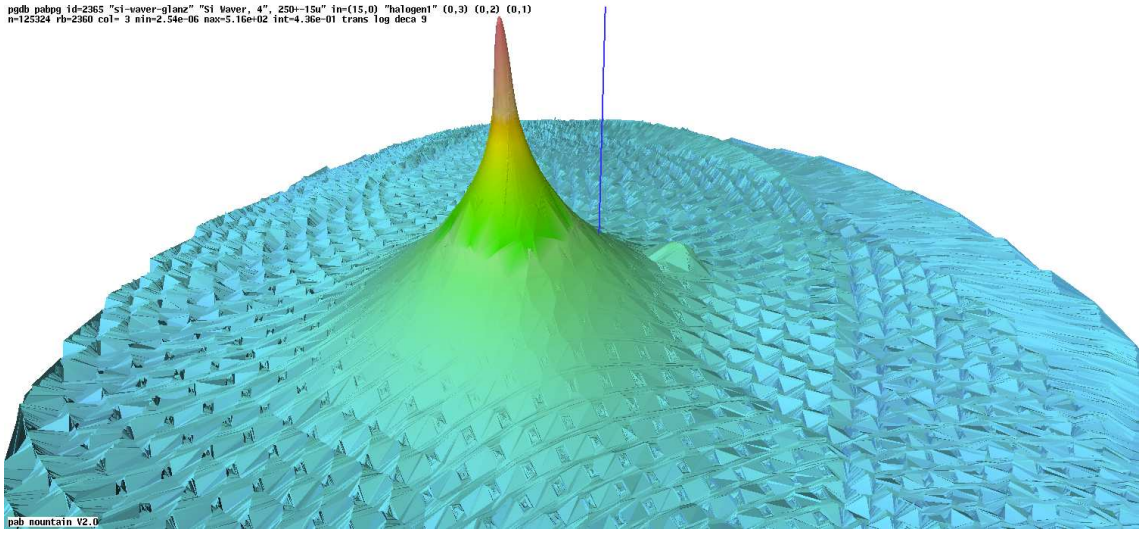


Figure 18. BRTFc infrared transmission of Si wafer at 2um for $\theta_{in} = 15^o$.

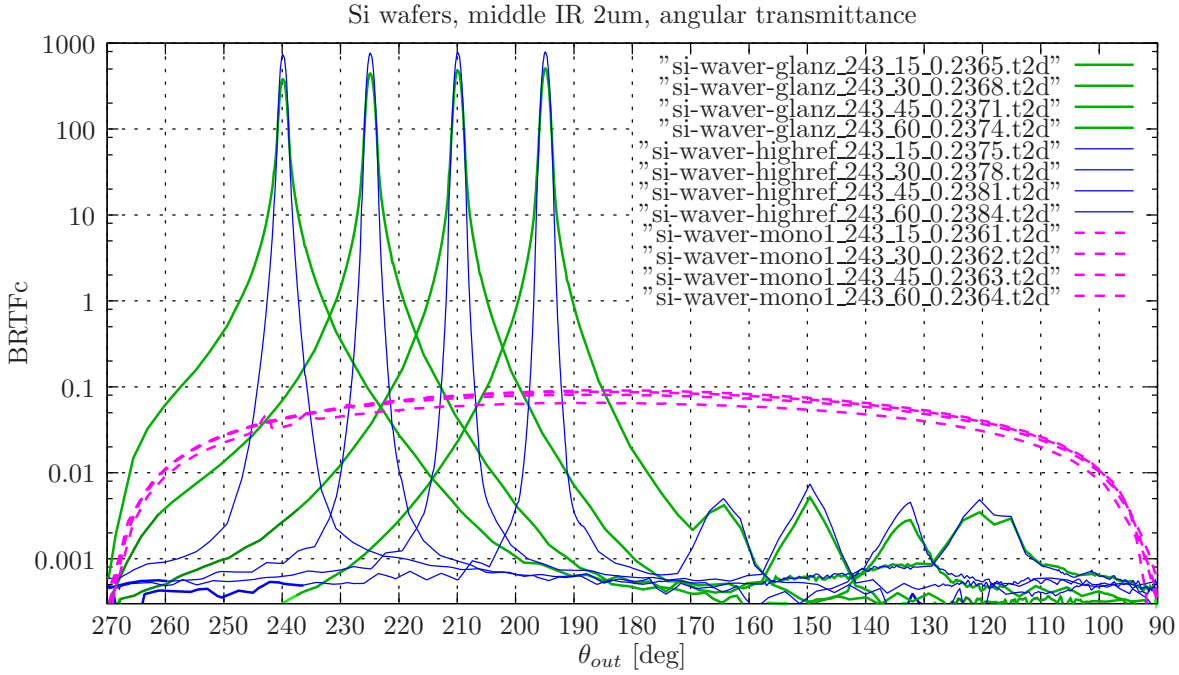


Figure 19. BRTFc infrared transmission of Si wafers at 2um for $\theta_{in} = 15, 30, 45, 60^o$. Two polished wafers of different surface treatment show low forward scattering, while a wafer with rougher finish scatters nearly diffusely.

Reflection BRTF in mid-IR and visible spectrum are shown in fig. 20. Specular peaks are increasing with $\theta_{in}$ in the infrared spectrum, but are not present in VIS spectrum.

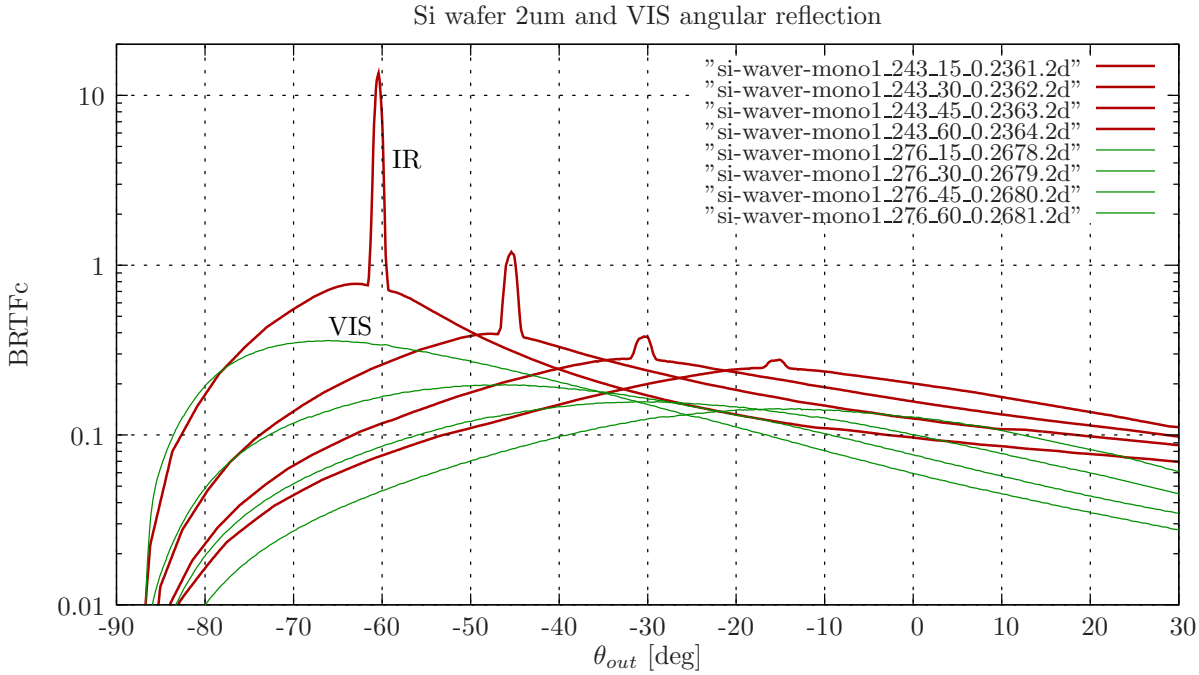


Figure 20. BRTFc reflection at Si wafer at 2um and in the visible spectrum (VIS) 400-700nm for $\theta_{in} = 15, 30, 45, 60^o$. Courtesy of samples: Fraunhofer-ISE, 2010, Dr. Glunz

## 4. VALIDATION

Two validation methods exists: Comparison with external measurement devices (includes "reference" samples) and implicit cross-checks within a device. External checks of the pgII include comparison to calibrated pico-amperemeters, comparison of numerical integrated values to integrating spheres, checks for linear sensor response and round-robin comparisons between pgII gonio-photometers that take different lab settings into account.[18] For space constraints, the details of external checks are left to an additional publication.

The pgII set-up offers some multiple implicit cross-checks, which seem both unique and useful and that are detailed in the following section.

### 4.1 mechanical accuracy and precision

Mechanical precision is given by precision of core components and overall alignment. As reference, some core parameters are given in table 1. The high resolution prism measurements in section 3.3 match these data from component manufacturers. The backlash in armB gear, already minimised by gear type, was software corrected for the high resolution measurements. Considering that the reduction ratio in this specific pgII was the lowest one available for armB, that is considered within specifications. The armA axis has direct angular encoder, which eliminates backlash. An additional angle encoder for armB would be feasible for applications requiring a higher precision than described in section 3.3.

### 4.2 implicit crosschecks

Implicit cross-checks within a measurement device offer useful routine control of data during normal operations and provide checks if external references are not available or not trust-worthy. For the pgII, they are mainly based in geometrical symmetry and time invariance:

| | resolution/precision | accuracy |
|---|---|---|
| armA encoder | 2.3” | ± 5” |
| armB gear | 4.3” | ± 6” |
| sample $\theta$ | 4.3” | ± 6” |
| sample $\phi$ | 1.2’ | ± 20” |
| | type | opening angle |
| detector | 10x10mm | $0.57^o$ |
| | 1mm | 3.4’ |
| light source | Halogen, f=200mm | $1.1^o$ |
| | HeNe laser | 2’ |
| | type | temporal stability |
| light source | Halogen | <0.3% |
| | Laser (diode) | <0.2% |

Table 1. Parameters for mechanical resolution and accuracy of drive system in standard configuration, and opening angles, stability of light sources.

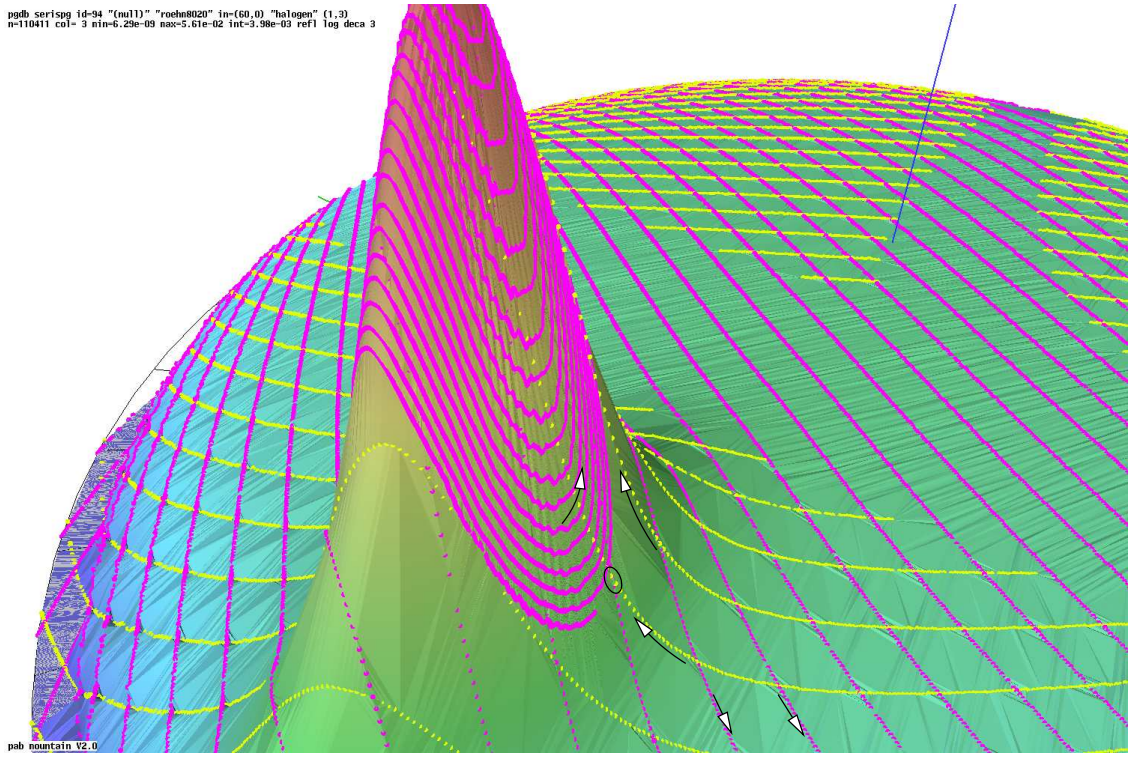


Figure 21. Slope of a peak structure in a BRTFc, showing *fullrot* paths matching paths generated by the *peak* scan method. Arrows indicate the scan direction. Time steps between measurement is 1ms, angular spacing between the two circled points is $0.3^o$ (logarithmic scale, 3 decades). Data courtesy of SERIS, NUS, Singapore, 2009.

The large number of data-points is probably the easiest and most useful cross-check in itself: The reconstructed BRTF from sampled BRTF points should be smooth, with all peaks being sampled by a sufficient number of measurement points. For each incident angle, a triangular mesh is constructed from measurement points using Delaunay triangulation. This serves as a robust way for any interpolation, and allows a fast and easy visualisation, as shown in fig.4: Scanning the BRTF with a coarse *fullrot* method under-samples the peak, which is sampled by one data-point only.
Data values of coarse scans match those of finer resolved scan data, since the time constants within the detector electronics are fast enough to capture the ”correct” value at any position. The match serves as cross-check that

time-delays within the analog/digital conversion in the order of a few microseconds are correctly compensated for. This is most easily shown at a steep slope of a peak flank, for example in fig. 21.

Each outgoing angle is reachable by two configurations of armA and armB. Comparison of data values for these two positions indicates alignment of axis, sensors and sensor-tubes. It also serves as indicator in the unlikely case that stray light is reflected off the arms onto the sample (shown in most plots in this paper and most clearly in fig. 21. Furthermore, each incident angle can be adjusted by two configurations of the sample axis, due to rotational symmetry around the incident axis. This serves as cross-check for alignment and influence of surrounding surfaces on stray light. Measurements with different lamps and identical sample should result in comparable data (apart from spectral influences and opening angles), since the unscattered beam of each lamp serves as reference. This is shown in fig. 7.

### 4.3 numerical integration and interpolation

Numerical processing of measured BRTF data is done for visualisation, integration, averaging and interpolation: Integration yields values in the range $[0:1]$ for the sum of direct-hemispherical transmission ($\tau_{dh}$) and reflection ($\rho_{dh}$), averaging does the same for constraint angular areas and interpolation transforms the BRTF to a matrix on a given $(\theta_{out}, \phi_{out})$ grid. Triangulation is the recommended method, since it avoids artifacts. Fig. 3 shows part of the triangulation, which blends all data-points into a surface for display and numerical uses.

Introduction to numerical integration of BRTF data is given in,[4] which used Voronoi cells for integration. The new integration uses the related Delaunay-triangles and is more robust. Tests have shown that the numerical integration is stable and robust for different point-distributions.

## 5. CONCLUSIONS

This paper introduces the pgII gonio-photometer in moderate detail and demonstrates its core ideas (section 2) and reachable precision with measured data of specular (section 3.3), metal (section 3.1) and near-ideal diffuse (section 3.2) materials. Both VIS and IR (2um) wavelength ranges are covered. Focus of this paper is on intrinsic checks, while [18] gives some external comparisons between pgII gonio-photometers.

It is faster then previous scanning gonio-photometers and has a simpler, more straight-forward layout then imaging gonio-photometers. This eases calibration and data validation. It uses the unscattered beam as reference and does not need external reference standards per-se, offering ab-initio BRTF values.

The pgII had been developed over a number of years, based on an earlier design and pgII machines are currently in use by research institutes and industrial clients. It is probably the first of its concept to combine specifically optimised layout, mechanics and custom electronics.

### 5.1 further work

Reduction in optical instrument signature (increasing the angular resolution by decreasing solid angles of detector and sources[19]) would extend capabilities towards measurement of stray light in imaging systems. In the other end of the scale, larger detector surfaces would further reduce measurement time of coarser data is sufficient, while still benefitting from the advantages of *one* moving sensor and the isotropic response on the sphere it provides. Both directions of development are feasible without changing the pgII basic mechanics.

Overall spectral response (section 3.3.4) may be measured with enhanced precision using standard gratings (based on previous ideas[14]) instead of the prism, which had been chosen for its transmission and reflection features.

Further noise reduction and extension of dynamic range are on the list of any measurement device, while fixed lower noise limits are imposed by $1/f$-noise, quantisation noise and other electronic noise sources. It seems worth noting that the current dynamic range is not using additional filters in the lamp subsystem.

The existing set-up may serve as a robust base for extending the measurement envelope, with BRTF data resolved per wavelength, polarisation or surface position as possible directions. Extending the covered wavelength range by other sources and detectors may be interesting.

All images are screen copies of the interactive BRTF visualisation program *mountain*. While some images have been rendered to facilitate easy reading of the printed grey-scale version, the amount of information is necessarily higher in a colour version. The reader is kindly directed to the PDF version.
prepared with LaTeX $2\varepsilon$, xfig, gnuplot et al, on Linux Debian

## REFERENCES


[1] R. Jacobson, *Applied Optics and Optical Engineering*, vol. 1, ch. Projection Screens, pp. 373 – 387. Academic Press, 1965.

[2] F. E. Nicodemus, J. Richmond, and J. Hsia, "Geometrical considerations and nomenclature for reflectance," tech. rep., U.S. Department of Commerce, National Bureau of Standards, October 1977.

[3] J. C. Stover, *Optical Scattering: Measurement and Analysis*, McGraw-Hill, 1990.

[4] P. Apian-Bennewitz and J. von der Hardt, "Enhancing and calibrating a goniophotometer," *Solar Energy Materials & Solar Cells* (54), pp. 309–322, 1998.

[5] J. C. Stover, "Overview of current scatterometer measurements and the impact on optical systems," in *Metrology of Optoelectronic Systems*, pp. 33–41, SPIE Vol 776, SPIE, 1987.

[6] P. Apian-Bennewitz, J. von der Hardt, and M. Goller, "Characterization of aerogels for computer simulations," in *Seventh Int. Meeting on: Transparent Insulation Technology*, Franklin Company, September 1994.

[7] M. Andersen, E. Stokes, N. Gayeski, and B. Browne, "Using digital imaging to assess spectral solar-optical properties of complex fenestration materials: A new approach to video-goniophotometry," *Solar Energy* **84**, pp. 549–562, 2010.

[8] L. E. Gilliam and R. A. Osiecki, "An in-vaccum br/tdf measurement apparatus," in *Stray Radiation V*, SPIE Vol 675, SPIE, 1986.

[9] G. J. Ward, "Measuring and modeling anisotropic reflection," in *Computer Graphics (SIGGRAPH '92 Proceedings)*, E. E. Catmull, ed., **26**, pp. 265–272, July 1992.

[10] K. M. Papamichael, J. Klems, and S. Selkowitz, "a large scanning radiometer for characterizing fenestration systems," Tech. Rep. LBL-24161, Lawrence Berkeley Laboratory, Workshop on optical property measurement techniques, Ispra, Italy, 27 Oct 1987, 1987.

[11] L. Mattson, "Instrument for angle-resolved measurement of scattered light in the vuv-visible wavelength region," in *Measurement and Effects of Surface Defects and Quality of Polish*, SPIE Vol 525, SPIE, 1985.

[12] P. Apian-Bennewitz, "Bau einer apparatur zur messung winkelabhängiger licht-streuung an anisotropen medien," Master's thesis, Universität Freiburg im Breisgau, April 1990.

[13] joule2 particpants, "Characterization of glazings materials for daylighting applications, final report," tech. rep., The Comission of the European Communities, CNRS ENTPE, Rue Audin, 69518 Vaulx-en-Velin, France, 1994.

[14] P. Apian-Bennewitz, *Messung und Modellierung von lichtstreuenden Materialien zur Computer-Simulation von Tageslichtbeleuchtung*. PhD thesis, Universität Freiburg, Fraunhofer Institut für solare Energiesysteme, D-79100 Freiburg, November 1995.

[15] Bergmann and Schäfer, eds., *Lehrbuch der Experimentalphysik*, vol. 3 Optik, Walter de Gruyter, 9 ed., 1993.

[16] M. Born and E. Wolf, *Principles of Optics*, Pergamon Press, 6 ed., 1987.

[17] T. F. Schiff, J. C. Stover, D. R. Cheever, and D. R. Bjork, "Maximum and minimum limitations imposed on bsdf measurements," in *Stray Light and Contamination in Optical Systems*, pp. 50–57, SPIE Vol. 967, 1988.

[18] L. O. Grobe, S. Wittkopf, P. Apian-Bennewitz, J. C. Jonsson, and M. Rubin, "Experimental validation of bidirectional reflection and transmission distribution measurements of specular and scattering materials," in *Photonics for Solar Energy Systems III*, R. B. Wehrspohn and A. Gombert, eds., SPIE Vol 7725, SPIE, May 2010.

[19] K. A. Klicker, J. C. Stover, D. R. Cheever, and F. M. Cady, "Practical reduction of instrumenent signature in near specular light scatter measurements," in *Current Developments in Optical Engineering II*, pp. 26–33, SPIE Vol 818, SPIE, 1987.